Single-Electron Qubits Based on Quantum Ring States on Solid Neon Surface

Toshiaki Kanai,[1,2] Dafei Jin,[3,*] and Wei Guo[1,4,†]
[1] *National High Magnetic Field Laboratory, 1800 East Paul Dirac Drive, Tallahassee, Florida 32310, USA*
[2] *Department of Physics, Florida State University, Tallahassee, Florida 32306, USA*
[3] *Department of Physics and Astronomy, University of Notre Dame, Notre Dame, Indiana 46556, USA*
[4] *Mechanical Engineering Department, FAMU-FSU College of Engineering, Tallahassee, Florida 32310, USA*

(Received 4 November 2023; accepted 23 May 2024; published 18 June 2024)

Single electrons trapped on solid-neon surfaces have recently emerged as a promising platform for charge qubits. Experimental results have revealed their exceptionally long coherence times, yet the actual quantum states of these trapped electrons, presumably on imperfectly flat neon surfaces, remain elusive. In this Letter, we examine the electron's interactions with neon surface topography, such as bumps and valleys. By evaluating the surface charges induced by the electron, we demonstrate its strong perpendicular binding to the neon surface. The Schrödinger equation for the electron's lateral motion on the curved 2D surface is then solved for extensive topographical variations. Our results reveal that surface bumps can naturally bind an electron, forming unique quantum ring states that align with experimental observations. We also show that the electron's excitation energy can be tuned using a modest magnetic field to facilitate qubit operation. This study offers a leap in our understanding of electron-on-solid-neon qubit properties and provides strategic insights on minimizing charge noise and scaling the system to propel forward quantum computing architectures.

DOI: 10.1103/PhysRevLett.132.250603

The success of quantum computing relies on qubits with long coherence times and swift operation [1,2]. Among various types of qubits, charge qubits are noted for their fast operation speeds, resulting from strong coupling to electric fields. However, traditional semiconductor and superconducting charge qubits face challenges with charge noise, which limits their coherence times to about 1 μs [3–5]. On the other hand, charge qubits composed of electrons bound to the surfaces of ultraclean quantum fluids and solids are predicted to exhibit prolonged coherence times [6–10]. Over the past two decades, significant advancements have been made in comprehending these systems [7,11–24]. In particular, in a recent breakthrough, electron-on-solid-neon (eNe) qubits were shown to achieve coherence times on the order of 0.1 ms, positioning them at the forefront of this endeavor [25,26].

The eNe qubit platform utilizes a hybrid quantum circuit structure consisting of a trap electrode placed inside a superconducting microwave resonator, accompanied by a number of guard electrodes, as shown schematically in Fig. 1(a) [25,26]. The trap electrode can be coated with a layer of solid neon. When an excess electron approaches the neon surface, the induced image charge in neon results in an attractive potential $V_\perp(z) = -[(\epsilon - \epsilon_0)/(\epsilon + \epsilon_0)]e^2/16\pi\epsilon_0 z$, where ϵ_0 is the vacuum permittivity, $\epsilon = 1.244\epsilon_0$ is the dielectric constant of solid neon, and z is the vertical distance from the flat surface. On the other hand, due to Pauli exclusion between the excess electron and the atomic shell electrons, the solid neon appears as an energy barrier of about 0.7 eV to the electron [27–30]. These combined effects confine the electron in the z direction with a ground-state wave function peaked at around 1 nm above the neon surface [see Fig. 1(b)].

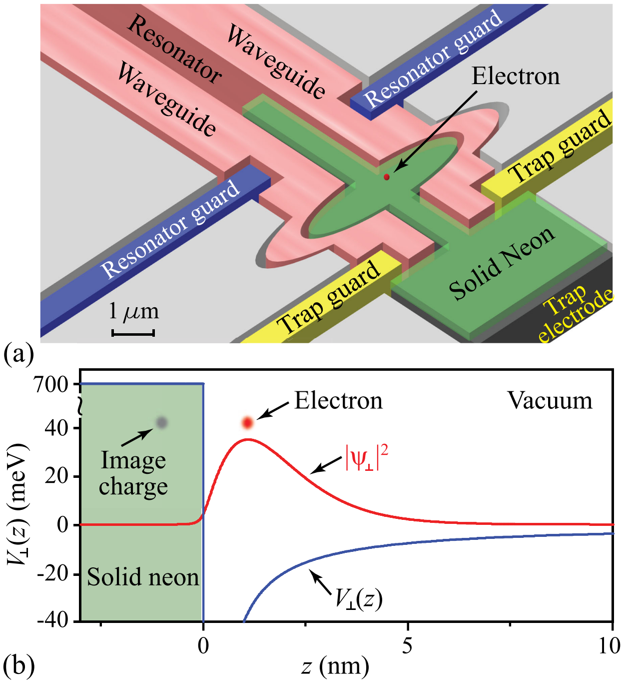

FIG. 1. (a) A schematic showing an electron trapped on the surface of solid neon in a superconducting microwave resonator. (b) Potential energy and the ground-state wave function of the electron near the flat solid-neon surface.

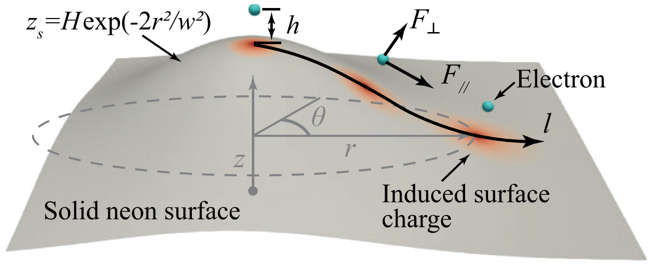

FIG. 2. A schematic showing the coordinate system adopted in our analysis of the electric forces acting on the electron near a curved solid-neon surface.

The ground-state energy is -15.8 meV, and the excitation energy to the first excited state in the z direction is about 12.7 meV, equating to an activation temperature of 147 K. At typical experimental temperatures around 10 mK, the electron's motion perpendicular to the surface remains firmly in the ground state. When suitable voltages are applied to the guard electrodes, the electron's lateral motion can be confined within the elliptical trap region depicted in Fig. 1(a). By adjusting these voltages, one can align the transition from the electron's lateral ground state to its first excited state with the resonator's microwave photons for qubit operations [25]. The electron, hovering in a near vacuum above the noble-element substrate, offers a qubit platform with minimal charge noise and hence exceptional coherence time. This qubit platform largely resolves the surface vibration and instability issues inherent in the electron-on-liquid-helium qubit platform, which was proposed over two decades ago [6,7] and has been extensively studied [7,13–24].

Nevertheless, recent experimental observations have revealed some intriguing behavior within the eNe qubit system. When the electric confining potential was reduced, the shift in the excitation spectrum associated with the electron's lateral motion was notably less than expected. Moreover, in some experimental runs, the electrons could remain anchored to the neon surface even after the confining potential was removed. These observations hint at the existence of alternative mechanisms affixing the electron on the neon surface. In this Letter, we consider the interaction between the electron and deformations on the neon surface, such as bumps and valleys. These surface features may arise from the Stranski-Krastanov growth mode of neon at temperatures below its triple point [31,32]. Additionally, electrodes made of superconducting niobium deposited on silicon substrates inherently possess their own surface irregularities. Our analysis demonstrates that small surface bumps can capture the electron, resulting in unique quantum ring states that align with the experimental observations.

Without loss of generality, we consider a Gaussian bump on the neon surface as shown in Fig. 2, defined by the position vector $\vec{r}_s = \vec{r}_s(r_s, \theta_s, z_s)$, with $z_s = H\exp(-2r_s^2/w^2)$. Here, H and w denote the bump's height and width, respectively. To evaluate the interaction between an excess electron and this surface bump, the key is to determine the surface charge density $\sigma(\vec{r}_s)$ induced by the electron. To achieve this, we adopt an adaptive polar mesh around the electron's location to discretize the bump surface (see Supplemental Material [33]). For a surface element $\Delta S(\vec{r}_s)$, the continuity of the electric displacement across the surface requires [34] $\epsilon_0[\vec{E}_e + \Delta\vec{E}_s + \sum_{\vec{r}_s' \neq \vec{r}_s} \Delta\vec{E}(\vec{r}_s')] \cdot \hat{n}_\perp = \epsilon[\vec{E}_e - \Delta\vec{E}_s + \sum_{\vec{r}_s' \neq \vec{r}_s} \Delta\vec{E}(\vec{r}_s')] \cdot \hat{n}_\perp$, where $\vec{E}_e = (-e/4\pi\epsilon_0) \times [(\vec{r}_s - \vec{r}_e)/(|\vec{r}_s - \vec{r}_e|^3)]$ is the electric field produced at $\vec{r}_s$ due to the electron located at $\vec{r}_e$, $\Delta\vec{E}_s = (\sigma(\vec{r}_s)/2\epsilon_0)\hat{n}_\perp$ denotes the electric field generated by the induced charge at ΔS itself with $\hat{n}_\perp$ as the unit vector normal to ΔS, and $\Delta\vec{E}(\vec{r}_s') = \{[\Delta S(\vec{r}_s')\sigma(\vec{r}_s')]/(4\pi\epsilon_0)\}[(\vec{r}_s - \vec{r}_s')/(|\vec{r}_s - \vec{r}_s'|^3)]$ is the electric field produced at $\vec{r}_s$ by a surface element at $\vec{r}_s'$. This condition leads to the following expression for $\sigma_s(\vec{r}_s)$:

$$\sigma(\vec{r}_s) = \frac{1}{2\pi}\frac{\epsilon - \epsilon_0}{\epsilon + \epsilon_0}\left[-e\frac{(\vec{r}_s - \vec{r}_e)}{|\vec{r}_s - \vec{r}_e|^3} + \sum_{\vec{r}_s{}' \neq \vec{r}_s} \Delta S(\vec{r}_s')\sigma(\vec{r}_s')\frac{(\vec{r}_s - \vec{r}_s')}{|\vec{r}_s - \vec{r}_s'|^3}\right] \cdot \hat{n}_\perp. \tag{1}$$

The above equation can be solved iteratively using an initial charge density $\sigma^{(0)}(\vec{r}_s) = (-e/2\pi)[(\epsilon - \epsilon_0)/(\epsilon + \epsilon_0)] \times [(\vec{r}_s - \vec{r}_e) \cdot \hat{n}_\perp/|\vec{r}_s - \vec{r}_e|^3]$, which is indeed the exact solution for a flat surface (see Supplemental Material [33]). In principle, for any given electron position $\vec{r}_e$, the associated surface charge density $\sigma(\vec{r}_s)$ should be determined. The electric potential energy of the electron can then be calculated as $V(\vec{r}_e) = \sum_{\vec{r}_s}(1/4\pi\epsilon_0)[-e\Delta S(\vec{r}_s)\sigma(\vec{r}_s)/|\vec{r}_s - \vec{r}_e|]$. This $V(\vec{r}_e)$, together with the 0.7-eV energy barrier from the curved neon surface, should be included in the Schrödinger equation for the electron to solve for its eigen wave functions in 3D space. However, this method is computationally intensive, limiting its feasibility for extensive investigations of diverse bump geometries.

Alternatively, we can calculate the electric force exerted on the electron due to the surface charge as $\vec{F}(\vec{r}_e) = \sum_{\vec{r}_s}\{[-e\Delta S(\vec{r}_s)\sigma(\vec{r}_s)]/4\pi\epsilon_0\}[(\vec{r}_s - \vec{r}_e)/(|\vec{r}_s - \vec{r}_e|^3)]$. From this, the forces parallel $\vec{F}_\parallel(\vec{r}_e)$ and perpendicular $\vec{F}_\perp(\vec{r}_e)$ to the local neon surface can be determined. For all the examined bump parameters $\{H, w\}$, we have found that $\vec{F}_\perp(\vec{r}_e)$ at any location above the curved neon surface only deviates minimally from the force on the electron from a flat surface (see Supplemental Material [33]). Therefore, the electron tends to bind at about 1 nm above the neon surface, exhibiting a distribution profile $|\psi_\perp(h)|^2$ perpendicular to the surface similar to that represented by the red curve in Fig. 1(b). This behavior is due to the bump surface's curvature radius being always substantially larger than 1 nm. Given this, we can focus on the electron's lateral

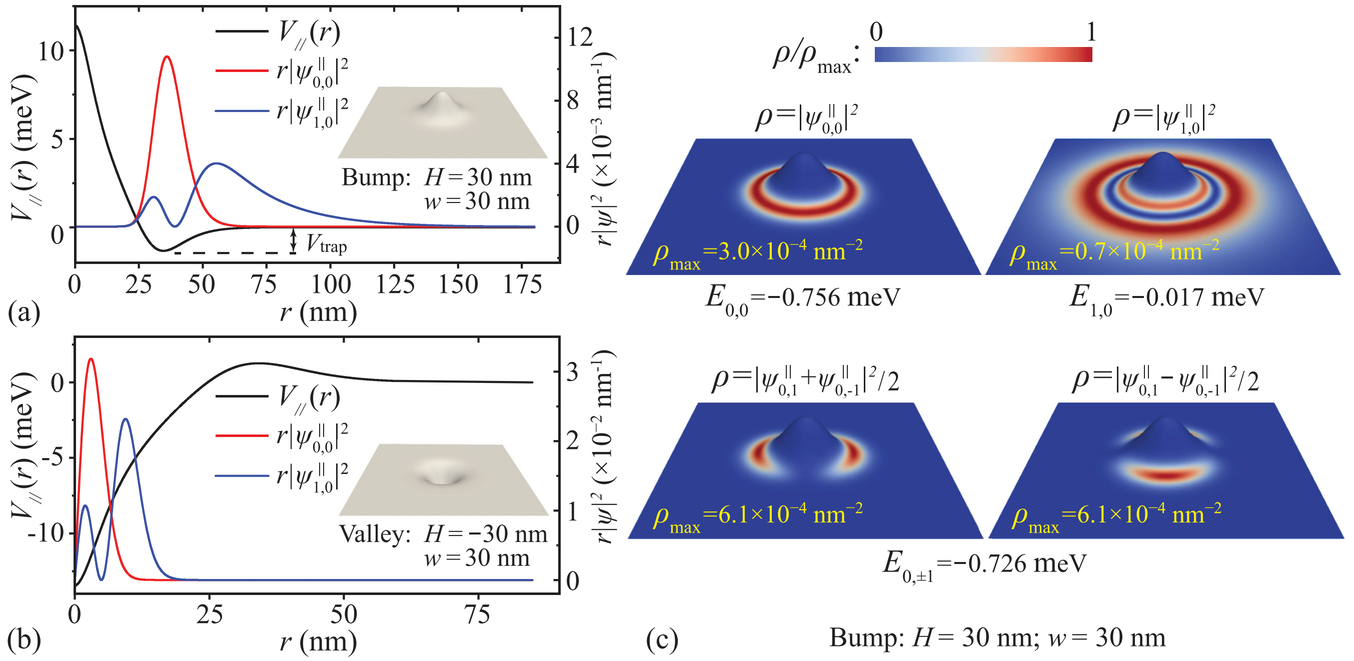

FIG. 3. (a) Potential energy profile associated with the electron's motion along a representative neon surface bump. The radial profiles of electron's wave function in its ground state and the first radially excited state are also shown. (b) Potential energy profile and the electron's radial wave function profiles along a representative neon surface valley. (c) 2D profiles of the ground state and excited states' wave functions of the electron bound to a surface bump with $H = 30$ nm and $w = 30$ nm.

motion along the curve neon surface, simplifying the 3D problem into a more manageable quasi-2D analysis.

Upon fixing the electron at a height h above the neon surface, the potential energy associated with the electron's lateral motion can be calculated as $V_{\|}(l) = \int_l^\infty \vec{F}_{\|}(l') \cdot d\vec{l'}$, where l is the coordinate mapped along the curved surface as shown in Fig. 2. Given the correlation between l and r, we can represent $V_{\|}$ in terms of r. Figure 3(a) shows the computed $V_{\|}(r)$ profile for the electron held at $h = 1$ nm above a representative neon bump with $H = 30$ nm and $w = 30$ nm. Notably, $\vec{F}_{\|}$ changes sign from negative at large r to positive at about $r = 34$ nm, which results in a toroidal trapping potential encircling the bump with a potential depth $V_{\text{trap}} = -1.33$ meV. This phenomenon can be explained by considering how the distance between the electron and the surface varies with l, as elucidated in the Supplemental Material [33]. Considering the likelihood $|\psi_{\perp}(h)|^2$ of the electron appearing at h, we have calculated $V_{\|}(r;h)$ at various h and averaged the results as $\overline{V_{\|}}(r) = \int V_{\|}(r;h)|\psi_{\perp}(h)|^2 dh$. It turns out that the averaged $\overline{V_{\|}}(r)$ profile shows little deviation from the curve displayed in Fig. 3(a), especially in the toroidal trap region (see Supplemental Material [33]). In subsequent analysis, we will fix the electron at $h = 1$ nm for convenient exploration of various bump geometries.

To find the eigenstates associated with the electron's lateral motion, we solve the following Schrödinger equation on the curved neon surface [35]:

$$\begin{aligned} E\psi_{\|}(r,\theta) &= -\frac{\hbar^2}{2m_e}\nabla^2\psi_{\|}(r,\theta) + V_{\|}(r)\psi_{\|}(r,\theta) \\ &= -\frac{\hbar^2}{2m_e r^2}\left[\frac{r}{h_r}\partial_r\left(\frac{r}{h_r}\partial_r\psi_{\|}\right) + \partial_\theta^2\psi_{\|}\right] \\ &\quad + V_{\|}(r)\psi_{\|}, \end{aligned} \tag{2}$$

where m_e is the electron mass, $\hbar$ is the reduced Planck's constant, and $h_r = \sqrt{1 + (16Hr^2/w^2)\exp[-(4r^2/w^2)]}$ is the Lamé coefficient for the Gaussian surface [36] (see Supplemental Material for derivation [33]). The wave function of an eigenstate can be expressed as $\psi^{\|}_{n_r,m_z}(r,\theta) = R_{n_r,m_z}(r)e^{im_z\theta}$, where n_r and m_z denote the radial and angular quantum numbers, respectively. Figure 3(a) displays the radial profiles of both the ground state $\psi^{\|}_{0,0}$ and the first radially excited state $\psi^{\|}_{1,0}$ of the electron over a bump with $H = 30$ nm and $w = 30$ nm. The probability densities of the electron on the bump surface and the eigenenergies E_{n_r,m_z} for these and two angularly excited states are shown in Fig. 3(c). Because of the geometry of the trapping potential, the eigenstates of the electron exhibit ring profiles around the bump.

We have also explored the interaction of the electron with valleys on the neon surface. Figure 3(b) shows the potential energy profile $V_{\|}(r)$ for an electron bound on a

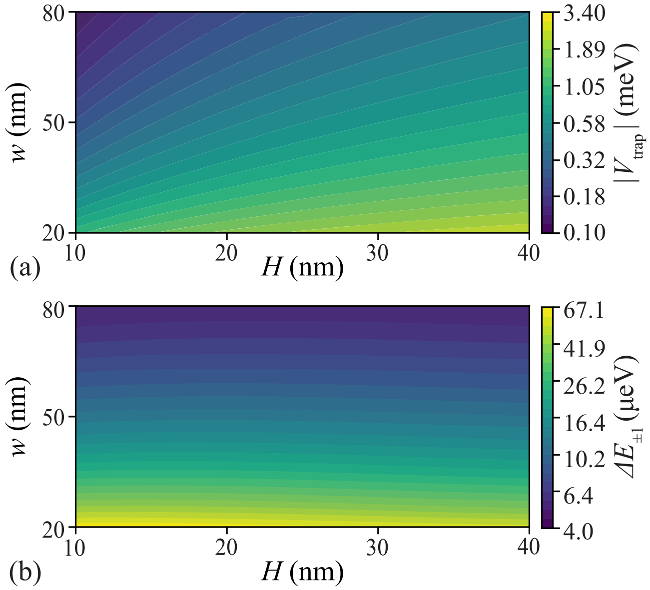

FIG. 4. (a) Trapping potential depth $|V_{\mathrm{trap}}|$ and (b) excitation energy $\Delta E_{\pm1} = E_{0,\pm1} - E_{0,0}$ for the electron on neon surface bumps with various H and w.

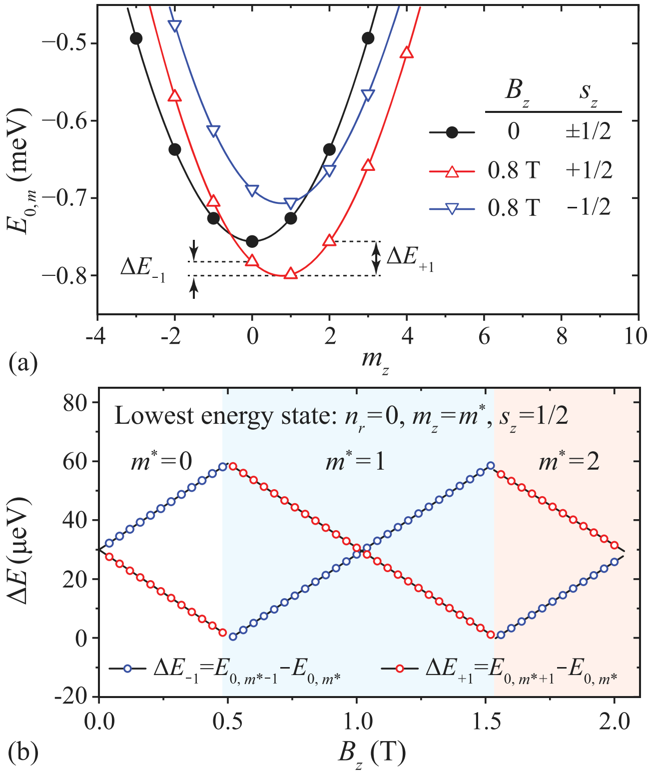

FIG. 5. (a) Eigenenergy versus angular quantum number m_z for the electron on a bump with $H = 30$ nm and $w = 30$ nm. (b) Calculated excitation energy $\Delta E_{\pm1}$ from the lowest energy state at m^* to the neighboring excited states at $m^* \pm 1$ as a function of the applied magnetic field B_z.

Gaussian-shaped valley with $H = -30$ nm and $w = 30$ nm, calculated using the same methodology applied for bumps. Given the inverse surface curvature as compared to the Gaussian bump shown in Fig. 3(a), the valley-associated potential is repulsive for $r \geq 34$ nm. For $r < 34$ nm, an axially symmetric potential well exists. The eigenstates of the electron confined in this potential well have been determined, with the radial profiles of the ground and the first radially excited states shown in Fig. 3(b). While such surface valleys can laterally confine the electron, they are not our primary focus. This is because when the electrons approach the solid neon, they adhere closely yet retain the ability to traverse the surface. From a distance, they are attracted to surface bumps but are repelled by valleys. Only upon exact positioning within the potential well region of the valleys is there a possibility of them becoming confined. Therefore, our subsequent analysis will focus on surface bumps.

We have investigated a wide range of parameter combinations $\{H, w\}$ for neon surface bumps. In Fig. 4(a), the derived trapping potential depth V_{trap} is presented as a function of H and w. The magnitude $|V_{\mathrm{trap}}|$ increases with increasing H or decreasing w and can reach a few meV, sufficient for electron confinement even in the absence of an applied electric trapping potential. Figure 4(b) displays the calculated excitation energy $\Delta E_{\pm1} = E_{0,\pm1} - E_{0,0}$ for an optical transition from the ground state $\psi_{0,0}$ to the degenerate excited states $\psi_{0,\pm1}$. Since this transition occurs between the standing wave modes along the circumference of the toroidal trapping potential, $\Delta E_{\pm1}$ depends strongly on w and is nearly independent of H. For bumps with w of about 32 nm, $\Delta E_{\pm1} \simeq 26$ μeV, matching well the energy of the microwave photons used in the experiments [25].

The degeneracy of the states $\psi_{0,1}$ and $\psi_{0,-1}$, which is unfavorable for qubit operation, can naturally be lifted if the bump lacks perfect axial symmetry. Alternatively, one can apply a magnetic field to remove this degeneracy and to align the excitation energy precisely with the resonator's photons. For an applied uniform magnetic field $\vec{B} = -B_z\hat{z}$, the eigenenergy of the electron is given by $E^{(s_z)}_{n_r,m_z} = E_r + (\hbar^2/2m_e)\langle 1/r^2\rangle m_z^2 - \mu_B B_z(m_z + 2s_z)$, where the radial energy contribution E_r is mildly influenced by m_z but strongly depends on n_r [35] (see Supplemental Material [33]), $\langle 1/r^2\rangle = \int 2\pi r dr[R^2_{n_r,m_z}(r)/r^2]$, $\mu_B = (e\hbar/2m_e)$ is the Bohr magneton, and $s_z = \pm\frac{1}{2}$ is the spin quantum number. In the absence of the magnetic field ($B_z = 0$), $E^{(s_z)}_{0,m_z}$ largely follows the trend $E^{(s_z)}_{0,m_z} - E^{(s_z)}_{0,0} \propto m_z^2$, with $\psi_{0,0}$ being the lowest energy state. Figure 5(a) shows the computed $E^{(s_z)}_{0,m_z}$ versus m_z for an electron confined on a bump with $H = 30$ nm and $w = 30$ nm. At finite B_z, the originally degenerate spin states now split. Furthermore, the linear term in m_z in the eigenenergy expression can cause a shift of the $E^{(s_z)}_{0,m_z}$ curve as shown in Fig. 5(a). Given the considerable bump size, $\langle 1/r^2 \rangle$ is small and hence the shift caused by the linear term in m_z can be significant, which may result in the lowest energy state with $m_z = m^* \neq 0$. The excitation energies $\Delta E_{-1} = E_{0,m^*-1} - E_{0,m^*}$ and $\Delta E_{+1} = E_{0,m^*+1} - E_{0,m^*}$ associated with the transitions from the new ground state at m^* to the two neighboring excited states at $m^* \pm 1$ now depend on B_z. In Fig. 5(b), we plot ΔE_{-1} and ΔE_{+1} as functions of B_z. The nearly linear dependence of $\Delta E_{\pm 1}$ on B_z suggests a robust capability of B_z to precisely adjust the qubit's transition frequency.

Our theoretical findings may have profound implications for the design and optimization of eNe qubits. In previous experiments, the injected electrons could bind to naturally formed bumps of various sizes. Only when an electron bound to a bump of the correct size and located within the resonator cavity, did its states become manipulable by the cavity photons. Electrons bound to neon bumps of mismatched sizes would fail to resonate with the cavity photons. But these electrons could contribute to background charge noise, potentially leading to qubit decoherence, limiting the coherence times of eNe qubits to about 0.1 ms. Our research underscores the critical need for a systematic study of the neon growth process under various injection temperatures and pressures, aimed at optimizing the procedure for producing high-quality neon surfaces with minimal natural features. This effort is anticipated to significantly reduce the number of background electrons and hence enhance the coherence times of eNe qubits. On the other hand, one may intentionally fabricate bumps of the right size on the trap electrode to enhance the chances of trapping electrons for qubit operation. These bumps could be elongated in the direction of the cavity electric field to lift the degeneracy of the $\psi_{0,1}$ and $\psi_{0,-1}$ states and enhance the dipole coupling to the cavity electric field. When two or more such bumps are fabricated so that multiple electrons can be trapped simultaneously, these electrons' lateral states could be manipulated and entangled using the cavity photons for various multiqubit gate applications. [37].

It is also worth noting that the application of a nonuniform magnetic field parallel to the neon surface can lead to coupling between the electron's lateral motion and its spin degrees of freedom [38]. Such a concept has previously been proposed for the electron-on-helium system [10,19,39,40] and implemented in other systems like silicon qubits [41–43]. The resonator's photons can be employed to stimulate and control the electron's spin states. A recent estimation suggests that the spin coherence time of the eNe qubit could extend up to 81 s when using purified neon [38]. The potential of constructing a fault-tolerant quantum computer leveraging the spin states of eNe qubits presents a compelling avenue for further research and development.

T. K. and W. G. acknowledge the support by the National Science Foundation under Grant No. DMR-2100790 and the Gordon and Betty Moore Foundation through Grant DOI 10.37807/gbmf11567. The work was conducted at the National High Magnetic Field Laboratory at Florida State University, which is supported by the National Science Foundation Cooperative Agreement No. DMR-2128556 and the state of Florida. D. J. acknowledges support from the Air Force Office of Scientific Research (AFOSR) under Grant No. FA9550-23-1-0636.

---

[*] dfjin@nd.edu

[†] wguo@magnet.fsu.edu

[1] R. Hanson, L. P. Kouwenhoven, J. R. Petta, S. Tarucha, and L. M. K. Vandersypen, Spins in few-electron quantum dots, Rev. Mod. Phys. **79**, 1217 (2007).

[2] N. P. De Leon, K. M. Itoh, D. Kim, K. K. Mehta, T. E. Northup, H. Paik, B. S. Palmer, N. Samarth, S. Sangtawesin, and D. W. Steuerman, Materials challenges and opportunities for quantum computing hardware, Science **372**, eabb2823 (2021).

[3] A. Chatterjee, P. Stevenson, S. De Franceschi, A. Morello, N. P. De Leon, and F. Kuemmeth, Semiconductor qubits in practice, Nat. Rev. Phys. **3**, 157 (2021).

[4] A. J. Heinrich, W. D. Oliver, L. M. K. Vandersypen, A. Ardavan, R. Sessoli, D. Loss, A. B. Jayich, J. Fernandez-Rossier, A. Laucht, and A. Morello, Quantum-coherent nanoscience, Nat. Nanotechnol. **16**, 1318 (2021).

[5] P. Stano and D. Loss, Review of performance metrics of spin qubits in gated semiconducting nanostructures, Nat. Rev. Phys. **4**, 672 (2022).

[6] P. M. Platzman and M. I. Dykman, Quantum computing with electrons floating on liquid helium, Science **284**, 1967 (1999).

[7] M. I. Dykman and P. M. Platzman, Quantum computing using electrons floating on liquid helium, Fortschr. Phys. **48**, 1095 (2000).

[8] S. A. Lyon, Spin-based quantum computing using electrons on liquid helium, Phys. Rev. A **74**, 052338 (2006).

[9] D. Jin, Quantum electronics and optics at the interface of solid neon and superfluid helium, Quantum Sci. Technol. **5**, 035003 (2020).

[10] E. Kawakami, J. Chen, M. Benito, and D. Konstantinov, Blueprint for quantum computing using electrons on helium, Phys. Rev. Appl. **20**, 054022 (2023).

[11] E. Kawakami, A. Elarabi, and D. Konstantinov, Image-charge detection of the Rydberg states of surface electrons on liquid helium, Phys. Rev. Lett. **123**, 086801 (2019).

[12] S. Zou and D. Konstantinov, Image-charge detection of the Rydberg transition of electrons on superfluid helium confined in a microchannel structure, New J. Phys. **24**, 103026 (2022).

[13] K. M. Yunusova, D. Konstantinov, H. Bouchiat, and A. D. Chepelianskii, Coupling between Rydberg states and landau levels of electrons trapped on liquid helium, Phys. Rev. Lett. **122**, 176802 (2019).

[14] F. R. Bradbury, M. Takita, T. M. Gurrieri, K. J. Wilkel, K. Eng, M. S. Carroll, and S. A. Lyon, Efficient clocked

electron transfer on superfluid helium, Phys. Rev. Lett. **107**, 266803 (2011).

[15] G. Sabouret, F. R. Bradbury, S. Shankar, J. A. Bert, and S. A. Lyon, Signal and charge transfer efficiency of few electrons clocked on microscopic superfluid helium channels, Appl. Phys. Lett. **92**, 082104 (2008).

[16] H. Byeon, K. Nasyedkin, J. R. Lane, N. R. Beysengulov, L. Zhang, R. Loloee, and J. Pollanen, Piezoacoustics for precision control of electrons floating on helium, Nat. Commun. **12**, 4150 (2021).

[17] E. Collin, W. Bailey, P. Fozooni, P. G. Frayne, P. Glasson, K. Harrabi, M. J. Lea, and G. Papageorgiou, Microwave saturation of the Rydberg states of electrons on helium, Phys. Rev. Lett. **89**, 245301 (2002).

[18] D. G. Rees, I. Kuroda, C. A. Marrache-Kikuchi, M. Höfer, P. Leiderer, and K. Kono, Point-contact transport properties of strongly correlated electrons on liquid helium, Phys. Rev. Lett. **106**, 026803 (2011).

[19] D. I. Schuster, A. Fragner, M. I. Dykman, S. A. Lyon, and R. J. Schoelkopf, Proposal for manipulating and detecting spin and orbital states of trapped electrons on helium using cavity quantum electrodynamics, Phys. Rev. Lett. **105**, 040503 (2010).

[20] G. Yang, A. Fragner, G. Koolstra, L. Ocola, D. A. Czaplewski, R. J. Schoelkopf, and D. I. Schuster, Coupling an ensemble of electrons on superfluid helium to a superconducting circuit, Phys. Rev. X **6**, 011031 (2016).

[21] G. Koolstra, G. Yang, and D. I. Schuster, Coupling a single electron on superfluid helium to a superconducting resonator, Nat. Commun. **10**, 5323 (2019).

[22] M. I. Dykman, P. M. Platzman, and P. Seddighrad, Qubits with electrons on liquid helium, Phys. Rev. B **67**, 155402 (2003).

[23] Y. P. Monarkha and S. S. Sokolov, Decay rate of the excited states of surface electrons over liquid helium, J. Low Temp. Phys. **148**, 157 (2007).

[24] E. Kawakami, A. Elarabi, and D. Konstantinov, Relaxation of the excited Rydberg states of surface electrons on liquid helium, Phys. Rev. Lett. **126**, 106802 (2021).

[25] X. Zhou, G. Koolstra, X. Zhang, G. Yang, X. Han, B. Dizdar, X. Li, R. Divan, W. Guo, K. W. Murch, D. I. Schuster, and D. Jin, Single electrons on solid neon as a solid-state qubit platform, Nature (London) **605**, 46 (2022).

[26] X. Zhou, X. Li, Q. Chen, G. Koolstra, G. Yang, B. Dizdar, Y. Huang, C. S. Wang, X. Han, X. Zhang, D. I. Schuster, and D. Jin, Electron charge qubit with 0.1 millisecond coherence time, Nat. Phys. **20**, 116 (2024).

[27] M. W. Cole and M. H. Cohen, Image-potential-induced surface bands in insulators, Phys. Rev. Lett. **23**, 1238 (1969).

[28] M. W. Cole, Properties of image-potential-induced surface states of insulators, Phys. Rev. B **2**, 4239 (1970).

[29] M. W. Cole, Electronic surface states of a dielectric film on a metal substrate, Phys. Rev. B **3**, 4418 (1971).

[30] D. Jin, Quantum electronics and optics at the interface of solid neon and superfluid helium, Quantum Sci. Technol. **5**, 035003 (2020).

[31] A. Esztermann, M. Heni, H. Löwen, J. Klier, M. Sohaili, and P. Leiderer, Triple-point wetting on rough substrates, Phys. Rev. Lett. **88**, 055702 (2002).

[32] V. Shchukin, N. Ledentsov, and S. Rouvimov, Formation of three-dimensional islands in subcritical layer deposition in Stranski-Krastanow growth, Phys. Rev. Lett. **110**, 176101 (2013).

[33] See Supplemental Material at http://link.aps.org/supplemental/10.1103/PhysRevLett.132.250603 for detailed discussions of the theoretical model and relevant simulation parameters.

[34] J. D. Jackson, *Classical Electrodynamics*, 3rd ed. (Wiley, New York, 1999).

[35] J. J. Sakurai and J. Napolitano, *Modern Quantum Mechanics*, 3rd ed. (Cambridge University Press, Cambridge, England, 2020).

[36] T. Y. Thomas, *Concepts from Tensor Analysis and Differential Geometry* (Academic Press, London, 1961).

[37] M. Veldhorst, C. H. Yang, J. C. C. Hwang, W. Huang, J. P. Dehollain, J. T. Muhonen, S. Simmons, A. Laucht, F. E. Hudson, K. M. Itoh, A. Morello, and A. S. Dzurak, A two-qubit logic gate in silicon, Nature (London) **526**, 410 (2015).

[38] Q. Chen, I. Martin, L. Jiang, and D. Jin, Electron spin coherence on a solid neon surface, Quantum Sci. Technol. **7**, 045016 (2022).

[39] M. Zhang and L. F. Wei, Spin-orbit couplings between distant electrons trapped individually on liquid helium, Phys. Rev. B **86**, 205408 (2012).

[40] M. I. Dykman, O. Asban, Q. Chen, D. Jin, and S. A. Lyon, Spin dynamics in quantum dots on liquid helium, Phys. Rev. B **107**, 035437 (2023).

[41] X. Mi, J. V. Cady, D. M. Zajac, P. W. Deelman, and J. R. Petta, Strong coupling of a single electron in silicon to a microwave photon, Science **355**, 156 (2017).

[42] X. Mi, M. Benito, S. Putz, D. M. Zajac, J. M. Taylor, G. Burkard, and J. R. Petta, A coherent spin–photon interface in silicon, Nature (London) **555**, 599 (2018).

[43] N. Samkharadze, G. Zheng, N. Kalhor, D. Brousse, A. Sammak, U. C. Mendes, A. Blais, G. Scappucci, and L. M. K. Vandersypen, Strong spin-photon coupling in silicon, Science **359**, 1123 (2018).